SUPPORTING INFORMATION

Low temperature atomic layer deposition of boron nitride using the in-situ decomposition of ammonium carbamate

Ana Álvarez-Yenes,*[ab] Victor O. Koroteev,[a] Maxim R. Ryzhikov,[c] Maxim Ilyn,[d] Svetlana G. Kozlova,[c] Mato Knez*[ae]

a CIC nanoGUNE BRTA, 20018 Donostia-San Sebastián, Basque Country, Spain

b University of the Basque Country UPV/EHU, 20018 Donostia-San Sebastián, Basque Country, Spain

c Nikolaev Institute of Inorganic Chemistry, Siberian Branch of Russian Academy of Science, 630090 Novosibirsk, Russian Federation

d Centro de Física de Materiales CSIC-UPV/EHU, 20018 Donostia-San Sebastián, Basque Country, Spain

e IKERBASQUE, Basque Foundation for Science. 48011 Bilbao, Basque Country, Spain

Experimental details

The ALD processes were performed in a commercial ALD reactor (Savannah S100 from Cambridge NanoTech Inc.). Nitrogen was used as a carrier gas. The deposition was performed under a constant flow of 20 standard cubic centimeters per minute (sccm) and a base pressure of the reaction chamber of 1 mbar. Boron tribromide (BBr_3, 99%, Acros Organics) was used as the boron source and ammonium carbamate ($[NH_4][H_2NCO_2]$, +99%, Sigma Aldrich) was used as the nitrogen source. BBr_3 was kept at room temperature during the deposition and ammonium carbamate was heated to 50°C to provide sufficient vapor pressure. The ALD experiments were carried out at 100 to 275°C reactor temperatures, with ALD cycles defined by 15 ms BBr_3 dosing, 5 s N_2 purge, 15 ms ammonium carbamate dosing and 10 s N_2 purge.

TEM characterization was carried out with a Cs-corrected microscope FEI Titan 60-300 (ThermoFisher, USA). The microscope was operated in monochromatic mode at an accelerating voltage of 300 kV.

The thicknesses of the samples were extracted from X-ray reflectivity (XRR) measurements performed with a PANalytical X'pert PRO diffractometer with a CuKα (λ=1.542 Å) radiation source and working voltage and current of 45 kV and 40 mA, respectively. Silicon (100) wafers were used as substrates. The thicknesses, densities and roughnesses of the films are fit using the python package xrayutilities.[1]

1. Growth per cycle studies of the self-limiting surface chemistry of the ALD process, performed at 250°C, as a function of the BBr_3 dosing times. The error bars at each point represent the data spread from Si wafers placed in different locations of the reaction chamber and different experiments, each point averages at least 4 measurements. The timing sequence used for the BBr_3 saturation experiment was X ms/5 s/15 ms/ 10 s (BBr_3 pulse/ N_2 purge/ ($[NH_4][H_2NCO_2]$ pulse/ N_2 purge), where X stands for a variable dosing time. The growth rate obtained remains constant as the dosing of the precursor is increased. This verifies the self-limiting nature of the film deposition. The dosing time of $[NH_4][H_2NCO_2]$ was set to 15 ms, minimum precision allowed by the reactor, due to the large pressure increase in the reaction chamber. Increasing the purge times did not alter the growth rates. Consequently, the timing sequence 15 ms/5 s/15 ms/10 s was used for all further experiments to fulfill a self-saturated condition for the studied ALD processes.

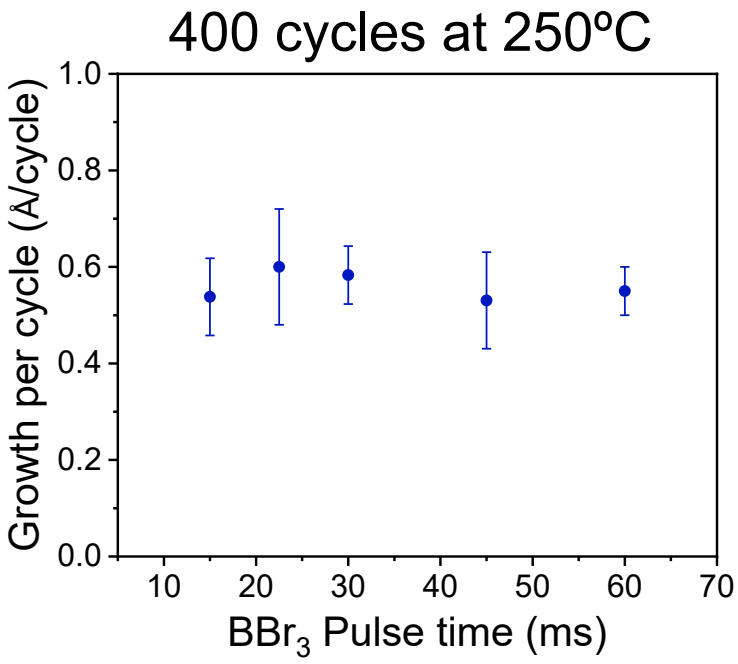

Figure S 1. Growth per cycle vs. BBr_3 dosing time at 250ºC.

2. Thickness vs. number of cycles of the studied process at 150ºC on sapphire substrates. GPC obtained from linear fit of 0.543 Å/cycle (r^2=0.99).

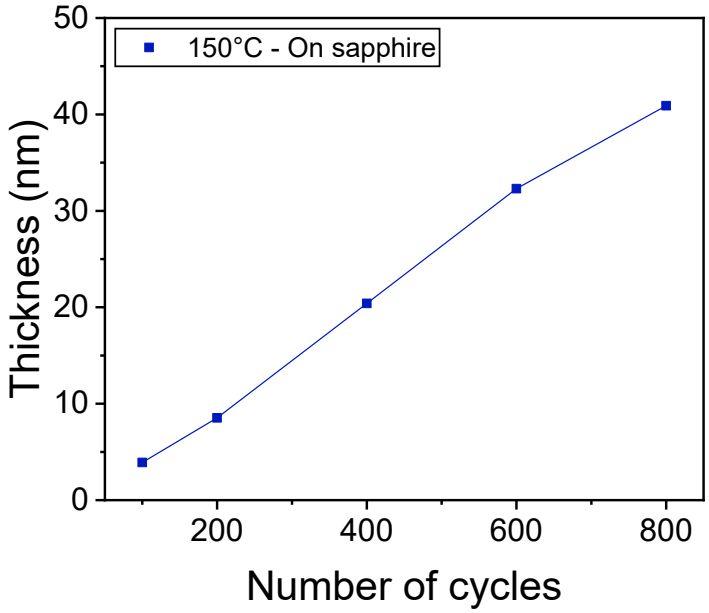

Figure S 2. Measured thicknesses of the deposited BN films vs. number of ALD cycles of BBr_3 and $[NH_4][H_2NCO_2]$ at 150°C on sapphire substrates.

3. XRR data and fit to a-BN for films grown from BBr_3 and ammonium carbamate on Si/SiO_2. The values of some of the thicknesses measured and fitted are validated through TEM imaging of the films.

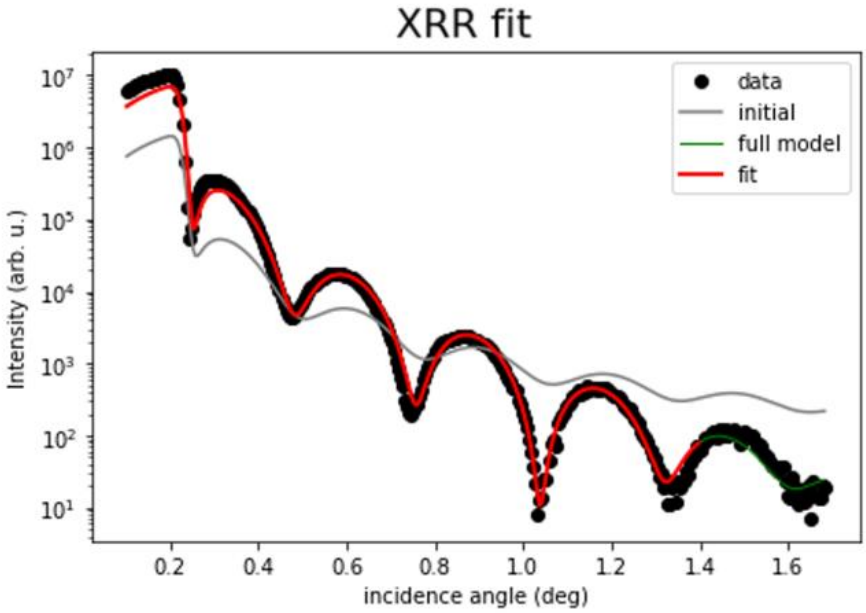

Figure S 3. XRR plot of a film deposited at 150°C with a measured thickness of 15.17 nm. The XRR data fit shows a thickness of 15.23 nm for the simulated a-BN thin film.

4. Densities of the thin films grown as a function of temperature, obtained from XRR fitting. Each point averages the density obtained for 3 different films of varying thicknesses. Densities obtained range from 1.73 to 1.78 gcm^{-3}. Mårlid et al.[2] reported densities of ALD-grown BN between 1.65 and 1.70 gcm^{-3} at 400°C.

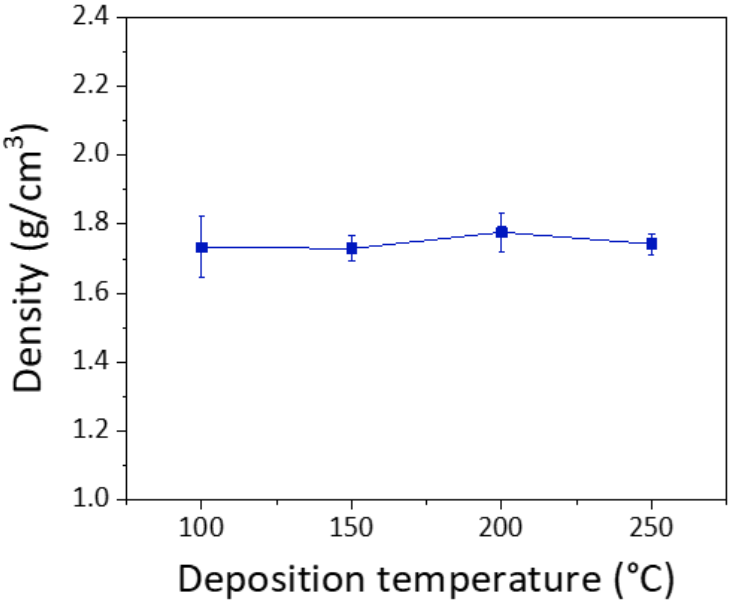

Figure S 4. Fitted density of the deposited BN films vs. deposition temperature.

5. Raman and XRD measurements, confirming the lack of long-range order in the deposited BN.

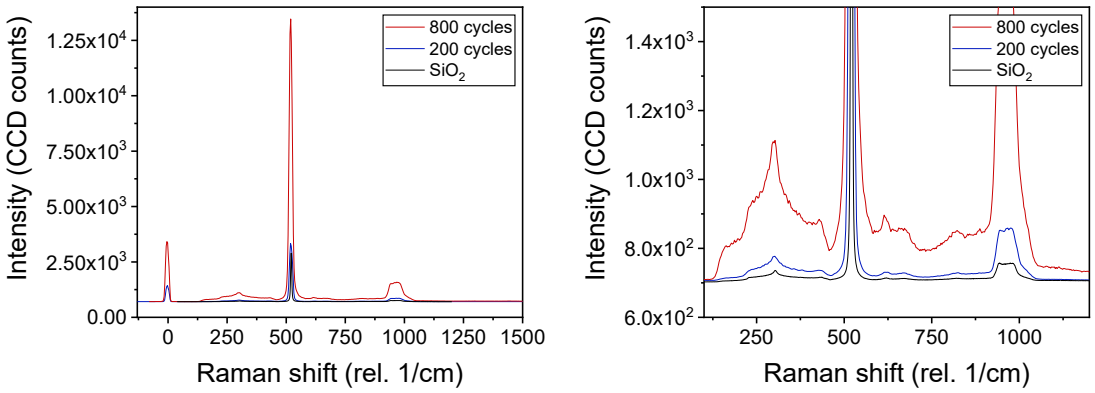

Figure S 5. Raman spectra of BN thin films deposited on SiO_2 at 250°C. The measured intensity increases with the number of cycles but the Raman spectrum of the SiO_2 substrate is identical to that of a-BN, suggesting that no distinct crystalline h-BN modes are present in a-BN. Similar results have been previously reported in CVD-grown a-BN films[3].

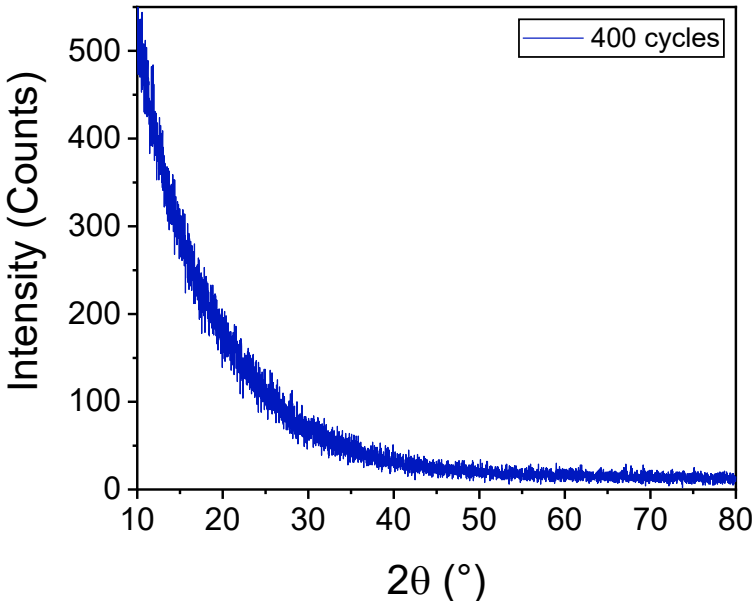

Figure S 6. GI-XRD pattern of a 25 nm thick BN film deposited at 150°C on a sapphire substrate. The absence of diffraction peaks confirms the lack of a crystalline structure.

6. Complete EELS mapping of the sample in Fig. 4.

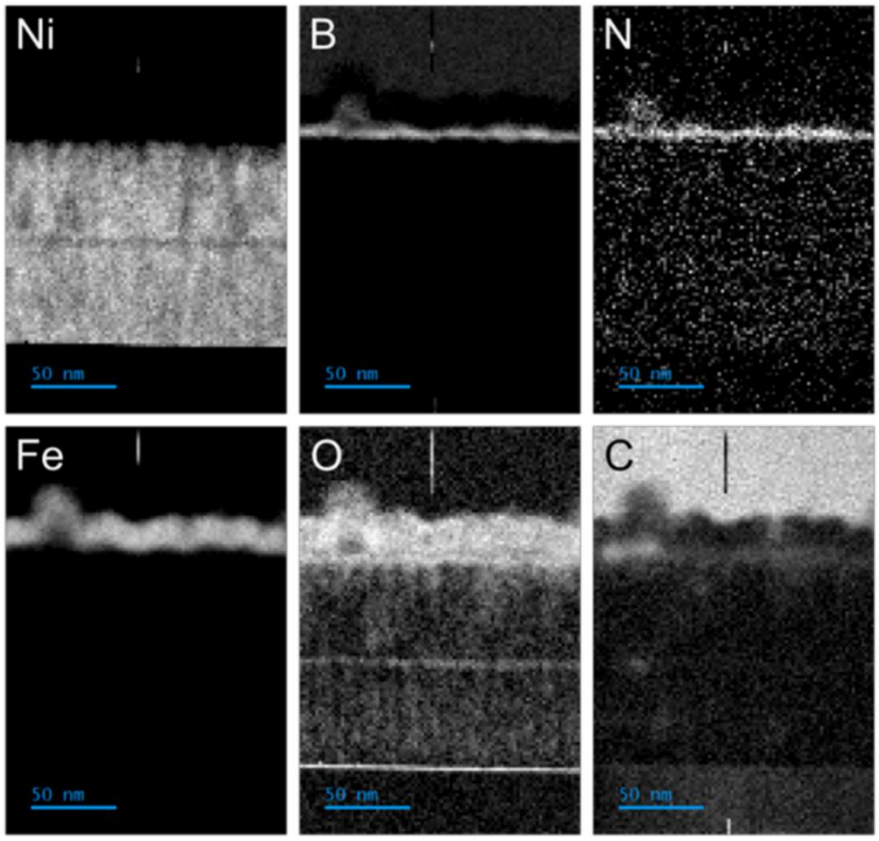

Figure S 7. EELS mapping of the elements found in a stack of 500 nm Ni/10 nm ALD BN/10 nm Fe. The ALD process was done at 150°C

Summary of prior ALD routes for the growth of Boron Nitride

Table S 1. Summary of prior ALD routes for the growth of Boron Nitride.

Reference	Precursor A	Precursor B		GPC (Å/cycle)	Temperature
Mårlid et al.[2] (2002)	BBr_3	NH_3		0.45	400 and 750°C
Ferguson et al.[4] (2002)	BCl_3	NH_3		~ 1	226,85 °C
Olander et al.[5] (2005)	BBr_3	NH_3	Thermal / laser assisted ALD	0.45/1.2	250-750 °C
Park et al.[6] (2017)	Tris(ethylmethylamino) borane ($C_9H_{24}BN_3$)	NH_3 + N_2 plasma	Plasma enhanced ALD	1.1	250–350 °C
Weber et al.[7] (2017)	BBr_3	NH_3		0.8	750 °C
Hao et al.[8] (2017)	Trichloroborazine ($B_3N_3H_3Cl_3$)	Hexamethyldisilazane ($NH(SiMe_3)_2$)		1.8	80 °C
Sprenger et al.[9] (2018)	Borazine ($B_3N_3H_6$)	Electrons	Electron enhanced ALD	1.5-3.0	27 and 100°C

XPS data and peak deconvolution

X-ray photoelectron spectroscopy (XPS) measurements were carried out with a Phoibos 100 photoelectron spectrometer, using a non-monochromatic Al−Kα X-ray source in the ultra-high vacuum chamber (base pressure $5x10^{-10}$ mbar). The analyzer energy resolution is 0.1 eV. Before the XPS measurements, the sample was sputtered with 500 eV Ar ions for 5 minutes. The estimated thickness of the removed layer is 1-2 nm. Data treatment consisted in a Shirley background subtraction and fitting of the peaks with a combination of Voigt functions (Python lmfit routine[10]). Results are presented in Table S2. The number of peak components and the naming follow the scheme proposed in [11]. Positions and parameters of each component were obtained from the fitting procedure with the limitations specified in Table S3. Insulating layer of aBN is prone to charging, therefore the plotted energy values are shifted by 1.2 eV, which gives reasonable coincidence of the main components of all peaks with the values listed in [11]. Decomposition of the Si 2s peak closely resembles results obtained in the work.[12] Broad O 1s, C 1s and B 1s peaks overlap with the ghost peaks caused by emission from Al−Kα3 and Al−Kα4 satellites of the non-monochromatic X-ray gun.[13] Therefore, acquisition of the data was performed in the wider range of energies and the ghost-peaks were included in the fitting procedure. In the case of B 1s, the ghost peak is too big and it probably overlaps with Br 3p1/2 line situated at 182 eV.[13]

Integrated peak areas I and respective sensitivity factors[5] S included in the Table S1 allow for calculation of the relative atomic fraction of the elements X_i and X_j via the equation[5]:

$$X_i : X_j = I_i/S_i : I_j/S_j \, .$$

For instance, the BN stoichiometry obtained from the area of the main components of the boron B-N and nitrogen N-B peaks is:

$$B{:}N = 6.486/0.159 : 18.540/0.477 = 1.05$$

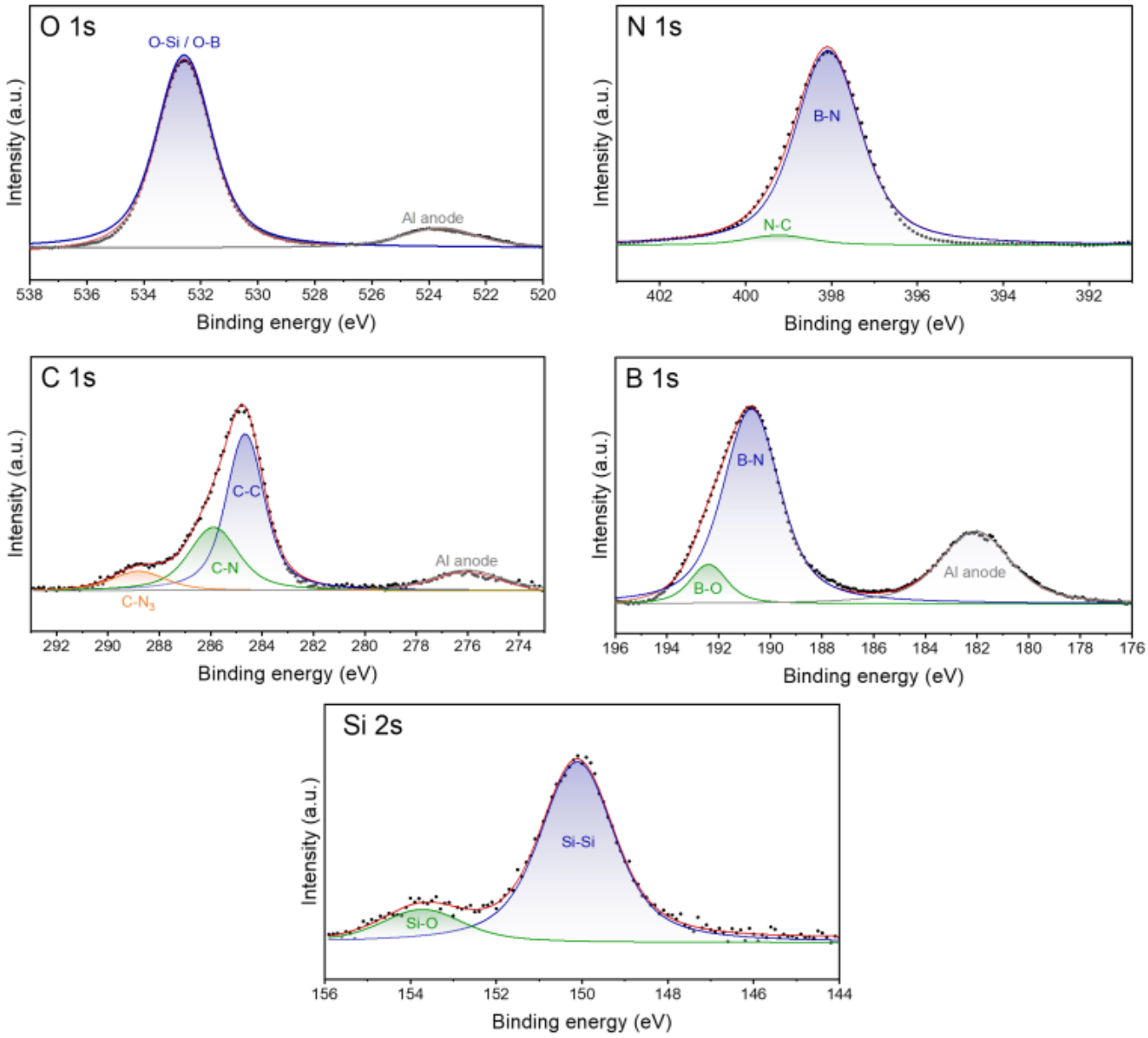

Figure S 8. Peak deconvolution and fitting of the XPS spectra.

Table S 2. Peak deconvolution values for the XPS results.

Element	Bond	Peak center (eV)	FWHM (eV)	I (a.u.)	Sensitivity factor[5]
O	O-B / O-Si	532.58	2.29	34.682	0.711
	Al sat	527.63	3.24		
N	N-C	399.23	1.80	0.946	0.477
	N-B	398.08	1.80	18.540	
C	$C\text{-}N_3$	288.81	2.46	0.588	0.296
	C-N	285.89	2.28	1.816	
	C-C	284.66	1.75	3.487	
	Al sat	276.02	3.24		
B	B-O	192.39	1.69	0.858	0.159
	B-N	190.73	2.61	6.486	
	Al sat + Br 3p1/2	182.07	3.24		
Si	Si-O	153.72	2.28	1.268	0.339
	Si-Si	150.11	2.05	0.252	

Table S 3. Limits for the fitting parameters.

Boundary/Element	**B 1s**	**C 1s**	**N 1s**	**O 1s**	**Si 2p**
Sigma Peak 1	0-0.9	0-0.55	0-0.5	open	open
Center Peak 1 (eV)	190-195	284-288	398-402	530-540	149-154
FWHM Peak 1 (eV)	0-3.24	0-1.98	0-1.8	open	open
Sigma Peak 2	0-0.9	0-0.9	0.5-0.9	0-0.9	0-0.9
Center Peak 2 (eV)	180-185	275-280	400-401	523-526	154-158
FWHM Peak 2 (eV)	0-3.24	0-3.24	1.8-3.24	0-3.24	0-3.24
Sigma Peak 3	0.3-0.8	0.3-0.8			
Center Peak 3 (eV)	193-195	290-293			
FWHM Peak 3 (eV)	1.08-2.88	1.08-2.88			
Sigma Peak 4		0.1-0.8			
Center Peak 4 (eV)		287-289			
FWHM Peak 4 (eV)		0.36-2.88			

Computational details

The calculations of the model systems were performed within ADF engine of the AMS2023 program suite.[14] The TPSSh meta-hybrid density functional,[15] Grimme D4(EEQ) dispersion correction,[16] all-electron Slater Type Orbitals QZ4P basis set[17] and Zero Order Regular Approximation (ZORA) for scalar relativistic effects[18] were used in all calculations. The frequencies and the Gibbs free energies at 100°C were calculated to identify the local minima and the transition states of the model reactions. The Intrinsic Reaction Coordinate (IRC) method[19] was used to link the reagents, transition states and products of the model reactions. The transition state theory equation ($k = (k_B T/h) * \exp(-\Delta G/RT)$) was used to calculate the rate constants from Gibbs energy differences of the transition states (Table S4) and the Gibbs energies of activation and rate constants (Table S5).

The optimized coordinates are provided in Tables S6-S17.

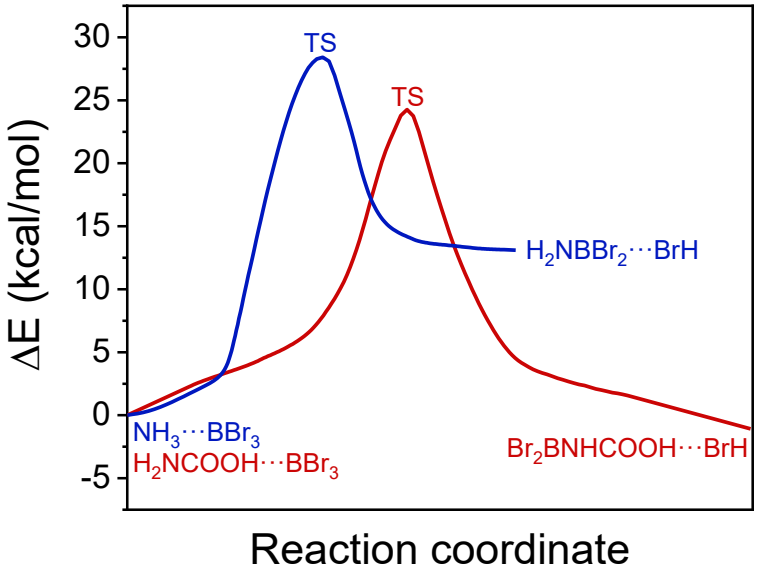

Figure S 9. IRC energy profiles calculated at the TPSSh+D4/QZ4P theoretical level from the transition states.

Table S 4. Gibbs energies (G, kcal/mol) and Gibbs energy differences (ΔG, kcal/mol) calculated at the TPSSh+D4/QZ4P theoretical level. The ΔG values are provided relative to the $NH_3\cdots BBr_3$ and $H_2NCOOH\cdots BBr_3$ pre-reaction complexes.

	$H_2NCOOH + BBr_3 \rightarrow Br_2BNHCOOH + BrH$			$NH_3 + BBr_3 \rightarrow H_2NBBr_2 + BrH$		
		G	ΔG		G	ΔG
Reagents	$H_2NCOOH + BBr_3$	-1474.94	-8.06	$NH_3 + BBr_3$	-875.08	11.76
Pre-reaction	$H_2NCOOH\cdots BBr_3$	-1466.88	0	$NH_3\cdots BBr_3$	-886.84	0
Transition state	$Br_2B\cdots NHCOOH\cdots BrH$	-1446.83	20.05	$H_2N\cdots BBr_2\cdots BrH$	-863.04	23.80
Post-reaction	$Br_2BNHCOOH\cdots BrH$	-1471.58	-4.70	$H_2NBBr_2\cdots BrH$	-879.49	7.35
Products	$Br_2BNHCOOH + BrH$	-1479.5	-12.62	$H_2NBBr_2 + BrH$	-888.61	-1.77

Table S 5. Calculated Gibbs energies of activation (ΔG) and rate constants (*k*) for the two model reactions.

Reaction	ΔG (kcal/mol)	*k* (Hz)
$H_2NCOOH\cdots BBr_3 \rightarrow Br_2BNHCOOH\cdots BrH$	20.05	14.0566
$NH_3\cdots BBr_3 \rightarrow H_2NBBr_2\cdots BrH$	23.80	0.0895

Table S 6. Cartesian coordinates of H_2NCOOH optimized at TPSSh+D4/QZ4P theoretical level.

N	1.37197839517607	-0.41222241715556	0.04142650202347
O	0.08240766466278	1.43388205108690	0.45495251308858
O	-0.85264421427128	-0.60940577133489	0.12706424825579
C	0.20182061445929	0.24864172176425	0.23861261019977
H	1.38568179043683	-1.41669565746727	0.03051770313998
H	2.22069727449906	0.08134692104235	0.25021374522543
H	-1.64292743863743	-0.06533812939185	0.24732935938132

Table S 7. Cartesian coordinates of NH_3 optimized at TPSSh+D4/QZ4P theoretical level.

N	0.09945576488707	0.22945187679185	-0.14589267013256
H	0.19835679422432	-0.63408249066210	-0.67049987407114
H	0.58798269978323	0.08940605975223	0.73296767247344
H	-0.88579525889461	0.31522454411801	0.08342486173024

Table S 8. Cartesian coordinates of BBr_3 optimized at TPSSh+D4/QZ4P theoretical level.

B	-0.25131721582439	-0.00094445742233	-4.53006106473293
Br	-0.25082808321180	1.38583213532050	-5.83026735826066
Br	-0.76987310072338	-1.76289500980814	-5.01985641003281
Br	0.26760986375958	0.37800733090996	-2.74101917097361

Table S 9. Cartesian coordinates of $H_2NCOOH\cdots BBr_3$ optimized at TPSSh+D4/QZ4P theoretical level.

N	1.01904020693291	-0.75828569129064	-0.26572693968562
O	0.96241313495114	0.83575995640674	1.43297542820942
O	-0.92315675945397	0.30124092810067	0.28281426143853
C	0.36439597270512	0.23518059491602	0.59584986041008
H	0.48628410639188	-1.63007288260636	-0.28506119824285
H	1.94216338643481	-0.93880068732063	0.12923625524733
H	-1.32642091043720	0.99752190224429	0.82490443285452
B	1.25423374512188	-0.35891738424023	-1.87327399574730
Br	1.68097120661844	1.57683343115855	-1.94052699491686
Br	-0.42330067509756	-0.85216439555338	-2.82257527152828
Br	2.79755068776337	-1.53957197595692	-2.36850405795891

Table S 10. Cartesian coordinates of $NH_3\cdots BBr_3$ optimized at TPSSh+D4/QZ4P theoretical level.

N	1.70725416071571	-0.85776846624276	-1.48627637388792
H	2.62969296893431	-1.12380693094725	-1.82900873914263
H	1.48028022053120	0.07084371480005	-1.84031596265702
H	1.02060585473934	-1.52175448587057	-1.84247012729890
B	1.69373127197759	-0.85639647252483	0.12447920942170
Br	3.07863256591855	0.48233153903851	0.66107964989382

Br	2.15735706559760	-2.72863343594994	0.65253209185087
Br	-0.16510776590312	-0.32091733328694	0.63092423364602

Table S 11. Cartesian coordinates of the transition state for the $H_2NCOOH\cdots BBr_3 \rightarrow Br_2BNHCOOH\cdots BrH$ reaction optimized at the TPSSh+D4/QZ4P theoretical level.

N	0.51711013241103	-0.54775216663147	-0.60494897949431
O	1.06231559516863	1.20258423019064	0.83297892215982
O	-0.83484054503629	-0.01281551910091	1.11209093524567
C	0.31475863119827	0.33584030634744	0.49441854961031
H	-0.26314276319016	-1.19072211182294	-0.71169782122176
H	1.61226876730354	-1.23075462015781	-0.45390330635614
H	-0.92514647751111	0.56457492854340	1.88548304455331
B	1.11976628047974	-0.13986583602323	-1.96721190677253
Br	1.78952672255108	1.61649146188516	-2.25125401886435
Br	0.34590987219608	-1.13637690609089	-3.42657134293060
Br	3.09564788483515	-1.59247997086645	-1.19927229462505

Table S 12. Cartesian coordinates of the transition state for the $NH_3\cdots BBr_3 \rightarrow H_2NBBr_2\cdots BrH$ reaction optimized at the TPSSh+D4/QZ4P theoretical level.

N	1.55882505804059	-0.07503370293044	-0.13189557621565
B	0.12588680047119	0.10031759870601	-0.56221974559717
H	1.99383095952262	-0.94464648087959	-0.42538601241957
H	1.30082276159100	-0.12573261536574	1.03978533065634
H	2.16517957290091	0.71866008113717	-0.31612464208118
Br	0.10097984760083	-0.09250251179143	2.38197570441440
Br	-0.82309713379120	-1.44903718907200	-1.10571892329694
Br	-0.48721422338903	1.86714736759242	-0.87605713928387

Table S 13. Cartesian coordinates of $Br_2BNHCOOH\cdots BrH$ optimized at the TPSSh+D4/QZ4P theoretical level.

N	-0.08773863399155	-0.18166560229473	-0.94703372761459
O	1.38018400610215	0.71004431414289	0.61279052929460
O	-0.60226824166990	-0.18164214488697	1.22326436000972
C	0.33691355558891	0.17448881807182	0.31928689608727
H	-0.94330269602727	-0.72136319723589	-0.93984741348906
H	2.93349955544940	-0.34226053519645	0.23498236191336
H	-0.25038744600686	0.05326792924366	2.09441049061197
B	0.46761062639291	0.12911672806420	-2.21861281198153
Br	1.95950804361813	1.26424903732504	-2.48660032453634
Br	-0.43194641169925	-0.64345595333569	-3.73001806556979
Br	3.86047294180371	-1.41663888648325	0.00445345385304

Table S 14. Cartesian coordinates of $H_2NBBr_2\cdots BrH$ optimized at the TPSSh+D4/QZ4P theoretical level.

N	1.41001049480190	-0.03257354380925	-0.35227977181083
B	0.16051291563836	0.12806076732222	-0.95086641413160
H	1.85125363460775	-0.93521469266478	-0.27002121041950
H	0.65689410221112	-0.10647673954204	1.67476169989394
H	2.01890853936249	0.74977880322899	-0.16955514388281
Br	0.31104292651595	-0.17931634839344	3.06349148410265

Br	-0.87090218859536	-1.41943755603335	-1.42658055613560
Br	-0.53353375119947	1.89444600861084	-1.23968939612276

Table S 15. Cartesian coordinates of $Br_2BNHCOOH$ optimized at the TPSSh+D4/QZ4P theoretical level.

N	-0.08860035738901	-0.15940071203964	-0.94607542680121
O	1.28167185593484	0.89848983316879	0.60345218846954
O	-0.54375990844190	-0.28478272661656	1.23564652001699
C	0.32584163077448	0.22816233615617	0.32434915963926
H	-0.92494030864264	-0.72791758275143	-0.93261910021615
Br	-0.43869532671692	-0.62491659019102	-3.73027452777720
H	-0.22527046466235	0.00280320003838	2.10359160807753
B	0.47930368657513	0.12550777229784	-2.21134998698931
Br	2.03726616757898	1.17298625904561	-2.48088968410147

Table S 16. Cartesian coordinates of H_2NBBr_2 optimized at the TPSSh+D4/QZ4P theoretical level.

N	1.43395599848606	-0.03122724119210	-0.40950458282084
B	0.17051328827552	0.12729877841778	-0.95181804614983
H	1.84312617769323	-0.93625714173410	-0.24426082280417
Br	-0.87910723352770	-1.41940372214911	-1.42130102420637
H	2.01253160269065	0.75006537692070	-0.14750953496533
Br	-0.54194059793809	1.89564465434632	-1.23463183622569

Table S 17. Cartesian coordinates of BrH optimized at the TPSSh+D4/QZ4P theoretical level.

Br	0.31310375988825	-0.18044299021520	3.05820521532293
H	0.65230732246721	-0.10753801619280	1.68097417549707

Supplementary References

1 D. Kriegner, E. Wintersberger and J. Stangl, *J Appl Crystallogr*, 2013, **46**, 1162–1170.

2 B. Mårlid, M. Ottosson, U. Pettersson, K. Larsson and J. O. Carlsson, *Thin Solid Films*, 2002, **402**, 167–171.

3 S. Hong, C. S. Lee, M. H. Lee, Y. Lee, K. Y. Ma, G. Kim, S. I. Yoon, K. Ihm, K. J. Kim, T. J. Shin, S. W. Kim, E. chae Jeon, H. Jeon, J. Y. Kim, H. I. Lee, Z. Lee, A. Antidormi, S. Roche, M. Chhowalla, H. J. Shin and H. S. Shin, *Nature*, 2020, **582**, 511–514.

4 J. D. Ferguson, A. W. Weimer and S. M. George, *Thin Solid Films*, 2002, **413**, 16–25.

5 J. Olander, L. M. Ottosson, P. Heszler, J. O. Carlsson and K. M. E. Larsson, *Chemical Vapor Deposition*, 2005, **11**, 330–337.

6 H. Park, T. K. Kim, S. W. Cho, H. S. Jang, S. I. Lee and S. Y. Choi, *Sci Rep*, DOI:10.1038/srep40091.

7 M. Weber, B. Koonkaew, S. Balme, I. Utke, F. Picaud, I. Iatsunskyi, E. Coy, P. Miele and M. Bechelany, *ACS Appl Mater Interfaces*, 2017, **9**, 16669–16678.

8 W. Hao, C. Marichy, C. Journet and A. Brioude, *ChemNanoMat*, 2017, **3**, 656–663.

9 J. K. Sprenger, H. Sun, A. S. Cavanagh, A. Roshko, P. T. Blanchard and S. M. George, *Journal of Physical Chemistry C*, 2018, **122**, 9455–9464.

10 M. Newville, T. Stensitzki, D. B. Allen and A. Ingargiola, *Zenodo*, 2014, preprint, DOI: 10.5281/zenodo.11813.

11 S. X. Li, T. Ichihara, H. Park, G. He, D. Kozawa, Y. Wen, V. B. Koman, Y. Zeng, M. Kuehne, Z. Yuan, S. Faucher, J. H. Warner and M. S. Strano, *Commun Mater*, DOI:10.1038/s43246-023-00345-8.

12 Y. J. Choi, S. J. Won, H. S. Jung, S. Park, D. Y. Cho, C. S. Hwang, T. J. Park and H. J. Kim, *ECS Solid State Letters*, DOI:10.1149/2.014201ssl.

13 J. F. Moulder and Jill. Chastain, *Handbook of X-ray photoelectron spectroscopy : a reference book of standard spectra for identification and interpretation of XPS data*, Perkin-Elmer Corp., Physical Electronics Division, Eden Prairie, Minn, 1992.

14 G. te Velde, F. M. Bickelhaupt, E. J. Baerends, C. Fonseca Guerra, S. J. A. van Gisbergen, J. G. Snijders and T. Ziegler, *J Comput Chem*, 2001, **22**, 931–967.

15 J. Tao, J. P. Perdew, V. N. Staroverov and G. E. Scuseria, *Phys Rev Lett*, 2003, **91**, 146401.

16 E. Caldeweyher, S. Ehlert, A. Hansen, H. Neugebauer, S. Spicher, C. Bannwarth and S. Grimme, *J Chem Phys*, 2019, **150**, 154122.

17 E. Van Lenthe and E. J. Baerends, *J Comput Chem*, 2003, **24**, 1142–1156.

18 E. van Lenthe, E. J. Baerends and J. G. Snijders, *J Chem Phys*, 1993, **99**, 4597–4610.

19 Carlos. Gonzalez and H. Bernhard. Schlegel, *J Phys Chem*, 1990, **94**, 5523–5527.